Tunable Phonon Polaritons in Atomically Thin van der Waals Crystals of Boron Nitride

S. Dai *et al.*

Science **343**, 1125 (2014);
DOI: 10.1126/science.1246833

nent from −45 nT to 40 nT in the geocentric solar magnetospheric (GSM) coordinate system. This coordinate system is defined such that the X axis points from Earth to the Sun, Y is perpendicular to Earth's magnetic dipole axis so that the XZ plane contains the dipole axis, and Z is in the same sense as the northern magnetic pole. For each magnetopause crossing, the magnetospheric density adjacent to the magnetopause was greater than 10 cm^{-3}. This is close to two orders of magnitude greater than the nominal value, demonstrating the presence of a plume. The density was measured through the spacecraft potential.

During each of the three magnetopause crossings, a strong rotation of the magnetic field (>120°) and a reconnection jet were observed. These crossings provide several confirmations of magnetic reconnection and the participation of the dense plume in the process. The first confirmation is the jet velocity. The reconnection jet is caused by the magnetic tension force that accelerates the exhaust plasma to the Alfvén speed. In the case of asymmetric reconnection, when the density and magnetic field strength are not the same on both sides of the current sheet, the jet velocity is a hybrid of Alfvén speeds on both sides. In each boundary crossing, the jet velocity matches to within 5% of the predicted hybrid Alfvén speed (Fig. 3) as calculated by a previous model (*9*, *16*).

A second confirmation of the impact of the cold plume plasma is the location of the reconnection jet. Typically the magnetosheath is much denser than the dayside magnetosphere and the jet lies primarily on magnetic field lines with magnetospheric orientation ($+B_L$) (*17*, *18*). In our study, the region of the magnetosphere adjacent to the magnetopause has been mass-loaded and the jets are primarily on field lines with magnetosheath orientation ($-B_L$) (Fig. 3). The occurrence of reconnection jets primarily on field lines of magnetosheath orientation provides additional evidence for the impact of the plume density on magnetopause reconnection.

The location of THEMIS at the reconnecting magnetopause also maps to the point in the ionosphere where the TOI is formed and enhancements in TEC stream tailward over the pole on open field lines (Fig. 1). This confirms that the formation of the TOI in the ionosphere is spatially linked to the presence of the plume and reconnection at the magnetopause. The dense plasma on newly opened magnetic field lines convects tailward over the pole, as observed in the motion of TOI patches in the ionosphere and in situ at the magnetopause. Future studies using the high spatial and almost continuous coverage of the ground-based TEC maps may use this connection to monitor reconnection and identify when plume material has reached the magnetopause.

In addition to identifying substantial density enhancements and mass loading at the magnetopause, these conjugate measurements confirm the connection between intermittent reconnection signatures at the magnetopause and in the ionosphere. Bursts of reconnection can cause twisted magnetic flux ropes known as flux transfer events to form at the magnetopause (*19*, *20*). At the magnetopause, a flux transfer event, demonstrating intermittent or "bursty" reconnection, was observed in the THEMIS measurements (Fig. 4). In the ionosphere, patches of TEC enhancements known as polar cap patches were observed convecting over the pole on open magnetic field lines (Fig. 1). These patches correspond to variability in reconnection causing uneven rates of plasma to be transported over the pole. Previous work (*13*, *14*) used polar cap patches to infer variability in magnetopause reconnection; however, this association had not been validated through in situ measurements at the magnetopause.

Our results imply an extended plasmaspheric plume that spanned from a nominal plasmapause to the dayside magnetopause, where it impacted magnetic reconnection. Ground-based TEC measurements demonstrate that the extended plume existed for several hours. During this period, three THEMIS spacecraft provided magnetically coincident measurements of the plume mass-loading the magnetopause reconnection site near local noon. The spacecraft measurements show signatures of intermittent or bursty reconnection at the magnetopause corresponding to the occurrence of patches of enhanced TEC convecting tailward on open field lines over the pole in the ionosphere. The simultaneous observation of the conjugate location of the reconnection site at the magnetopause with the TEC cusp signature ionosphere (Fig. 1) is important. With this association validated, studies of the occurrence, location, and variability of reconnection at the magnetopause can be conducted with the assistance of ground-based TEC maps that provide high spatial and almost continuous temporal coverage.

References and Notes

1. C. R. Chappell, K. K. Harris, G. W. Sharp, *J. Geophys. Res.* **75**, 50–56 (1970).
2. C. R. Chappell, K. K. Harris, G. W. Sharp, *J. Geophys. Res.* **76**, 7632–7647 (1971).
3. J. C. Foster, A. J. Coster, P. J. Erickson, F. J. Rich, B. R. Sandel, *Geophys. Res. Lett.* **31**, L08809 (2004).
4. J. C. Foster, P. J. Erickson, A. J. Coster, J. Goldstein, F. J. Rich, *Geophys. Res. Lett.* **29**, 1623 (2002).
5. J. E. Borovsky, M. H. Denton, *Geophys. Res. Lett.* **33**, L20101 (2006).
6. J. E. Borovsky, M. Hesse, *Phys. Plasmas* **14**, 102309 (2007).
7. B. M. Walsh, D. G. Sibeck, Y. Nishimura, V. Angelopoulos, *J. Geophys. Res.* **118**, 4844–4851 (2013).
8. J. E. Borovsky, M. H. Denton, R. E. Denton, V. K. Jordanova, J. Krall, *J. Geophys. Res.* **118**, 5695–5719 (2013).
9. P. A. Cassak, M. A. Shay, *Phys. Plasmas* **14**, 102114 (2007).
10. J. Birn, J. E. Borovsky, M. Hesse, *Phys. Plasmas* **15**, 032101 (2008).
11. J. C. Foster, *J. Geophys. Res.* **98**, 1675 (1993).
12. J. C. Foster *et al.*, *J. Geophys. Res.* **110**, A09S31 (2005).
13. Q. H. Zhang *et al.*, *Science* **339**, 1597–1600 (2013).
14. M. Lockwood, H. C. Carlson Jr., *Geophys. Res. Lett.* **19**, 1731–1734 (1992).
15. V. Angelopoulos, *Space Sci. Rev.* **141**, 5–34 (2008).
16. See supplementary materials on *Science* Online.
17. G. Paschmann *et al.*, *J. Geophys. Res.* **91**, 11099 (1986).
18. A. L. La Belle-Hamer, A. Otto, L. C. Lee, *J. Geophys. Res.* **100**, 11875 (1995).
19. C. T. Russell, R. C. Elphic, *Space Sci. Rev.* **22**, 681 (1978).
20. L. C. Lee, Z. F. Fu, *Geophys. Res. Lett.* **12**, 105–108 (1985).
21. J.-H. Shue *et al.*, *J. Geophys. Res.* **102**, 9497 (1997).
22. P. T. Newell *et al.*, *Ann. Geophys.* **20**, 1039–1047 (2002).

Acknowledgments: Supported by NSF grant AGS-1136827. We acknowledge NASA contract NAS5-02099 and instrument teams for use of the data from the THEMIS Mission, specifically the ESA, EFI, and FGM teams. Work at MIT Haystack Observatory was supported by NSF Cooperative Agreement AGS-1242204.

Supplementary Materials

www.sciencemag.org/content/343/6175/1122/suppl/DC1
Supplementary Text
Table S1
References (*23*–*26*)

15 October 2013; accepted 6 February 2014
10.1126/science.1247212

Tunable Phonon Polaritons in Atomically Thin van der Waals Crystals of Boron Nitride

S. Dai,[1] Z. Fei,[1] Q. Ma,[2] A. S. Rodin,[3] M. Wagner,[1] A. S. McLeod,[1] M. K. Liu,[1] W. Gannett,[4,5] W. Regan,[4,5] K. Watanabe,[6] T. Taniguchi,[6] M. Thiemens,[7] G. Dominguez,[7,8] A. H. Castro Neto,[3,9] A. Zettl,[4,5,10] F. Keilmann,[11] P. Jarillo-Herrero,[2] M. M. Fogler,[1] D. N. Basov[1]*

van der Waals heterostructures assembled from atomically thin crystalline layers of diverse two-dimensional solids are emerging as a new paradigm in the physics of materials. We used infrared nanoimaging to study the properties of surface phonon polaritons in a representative van der Waals crystal, hexagonal boron nitride. We launched, detected, and imaged the polaritonic waves in real space and altered their wavelength by varying the number of crystal layers in our specimens. The measured dispersion of polaritonic waves was shown to be governed by the crystal thickness according to a scaling law that persists down to a few atomic layers. Our results are likely to hold true in other polar van der Waals crystals and may lead to new functionalities.

Layered van der Waals (vdW) crystals consist of individual atomic planes weakly coupled by vdW interaction, similar to graphene monolayers in bulk graphite (*1*–*3*). These materials can harbor superconductivity (*2*) and ferromagnetism (*4*) with high transition

temperatures, emit light (*5*, *6*), and exhibit topologically protected surface states (*7*), among many other effects (*8*). An ambitious practical goal (*9*) is to exploit atomic planes of vdW crystals as building blocks of more complex artificially stacked structures where each such block will deliver layer-specific attributes for the purpose of their combined functionality (*3*). We explored the behavior of phonon polaritons in hexagonal boron nitride (hBN), a representative vdW crystal. The phonon polaritons are collective modes that originate from coupling of photons with optical phonons (*10*) in polar crystals. They have been investigated in the context of energy transfer (*11*, *12*), coherent control of the lattice (*13*), ultramicroscopy (*14*, *15*), "superlensing" (*16*), and metamaterials (*17*, *18*). Tunable phonon polaritons that we discovered in hBN by direct infrared (IR) nanoimaging set the stage for the implementation of these appealing concepts in vdW heterostructures. Polaritonic effects reported here are likely generic to other polar vdW solids because these materials commonly show optical phonons. hBN stands out in this class of materials thanks to its light constituent elements, which yield particularly strong phonon resonances that span a broad region of the technologically important IR band.

IR nanoimaging and Fourier transform IR nano-spectroscopy (nano-FTIR) experiments were performed at UCSD by using a scattering-type scanning near-field optical microscope (s-SNOM) (*19*). The physics of polariton imaging using s-SNOM is akin to nanoimaging of surface plasmons (*20*, *21*) (Fig. 1A). In short, we illuminated the metalized tip of an atomic force microscope (AFM) with an IR beam. We used quantum cascade lasers (QCLs) with tunable frequency $\omega = 1/\lambda_{IR}$, where λ_{IR} is IR beam wavelength and a broad-band difference frequency generation (DFG) laser system (*22*). Our AFM tip with curvature radius $a \approx 25$ nm is polarized by the incident IR beam. The light momenta imparted by the tip extend to the typical range of momenta supporting phonon polaritons in hBN (Fig. 2E). Therefore, the strong electric field between the tip and the sample provides the necessary momentum to launch polariton waves of wavelength λ_p that propagate radially outward from the tip along the hBN surface. AFM tips exploited in our nanospectroscopy instrument are commonly referred to as optical antennas (*23*): an analogy that is particularly relevant to describe the surface wave launching function of the tip. Upon reaching the sample edge, polaritonic waves are reflected back, forming a standing wave between the tip and hBN edge. As the tip is scanned toward the edge, the scattering signal collected from underneath the tip reveals oscillations with the period of $\lambda_p/2$.

Representative nanoimaging data are displayed in Fig. 1, B and D to F, where we plot the normalized near-field amplitude $s(\omega) = s_{hBN}(\omega)/s_{Au}(\omega)$ at several IR frequencies in the 1550- to 1580-cm^{-1} range. Here, $s_{hBN}(\omega)$ and $s_{Au}(\omega)$ are the scattering amplitudes for, respectively, the sample and the reference (Au-coated wafer) (*19*). The amplitudes were demodulated at the third or the fourth harmonic of the tapping frequency to isolate the genuine near-field signal (*23*). The images in Fig. 1, B to F, were taken for a tapered hBN crystal of thickness $d = 256$ nm. They reveal a hatched pattern of periodic maxima, fringes, of $s(\omega)$ running parallel to the edges, with the "hot spots" located where two or more fringes intersect. We observed similar fringe patterns in other hBN samples, including those that are only a few atomic layers thick (Fig. 1G). Such patterns are readily accounted for (Fig. 1C) within a phenomenological theory that considers reflections from the tapered edges (*19*).

Data in Fig. 1 allow one to obtain the polariton wavelength λ_p simply by doubling the fringe period, and the corresponding momentum can be calculated as $q = 2\pi/\lambda_p$. We used two approaches to determine the dispersion relation $q = q(\omega)$ of the polaritons. One method (*15*, *20*, *21*) is to analyze the periodicity of fringes at discrete frequencies of the IR source (Fig. 1, B and D to G). We have complemented this procedure with a technique capable of capturing the entire dispersion in the course of one single scan of our nanoscope. We executed this line scan on an hBN crystal with a large surface area to ensure that the $L = 0$ boundary is the principal reflector for the tip-launched polaritons (Fig. 2A). Such a line scan (Fig. 2, A, B, and D) is composed of a series of broad-band nano-FTIR spectra taken at every pixel. Starting in the region of unobscured SiO_2 substrate ($L < 0$) and continuing through the hBN crystal ($L > 0$), we combined the spectra from all pixels along the line scan and thus obtained a two-dimensional map $s(L, \omega)$, shown in Fig. 2B. In the plot, we observed a series of resonances that systematically vary with frequency ω and the distance from the sample edge

[1]Department of Physics, University of California, San Diego (UCSD), La Jolla, CA 92093, USA. [2]Department of Physics, Massachusetts Institute of Technology, Cambridge, MA 02139, USA. [3]Department of Physics, Boston University, Boston, MA 02215, USA. [4]Department of Physics, University of California, Berkeley, Berkeley, CA 94720, USA. [5]Materials Sciences Division, Lawrence Berkeley National Laboratory, Berkeley, CA 94720, USA. [6]National Institute for Materials Science, Namiki 1-1, Tsukuba, Ibaraki 305-0044, Japan [7]Department of Chemistry and Biochemistry, University of California, San Diego, La Jolla, CA 92093, USA. [8]Department of Physics, California State University, San Marcos, San Marcos, CA 92096, USA. [9]Graphene Research Centre and Physics Department, National University of Singapore, 6 Science Drive 2, Singapore 117546, Singapore. [10]Kavli Energy NanoSciences Institute at the University of California, Berkeley, and the Lawrence Berkeley National Laboratory, Berkeley, CA 94720, USA. [11]Ludwig-Maximilians-Universität and Center for Nanoscience, 80539 München, Germany.

*Corresponding author. E-mail: dbasov@physics.ucsd.edu

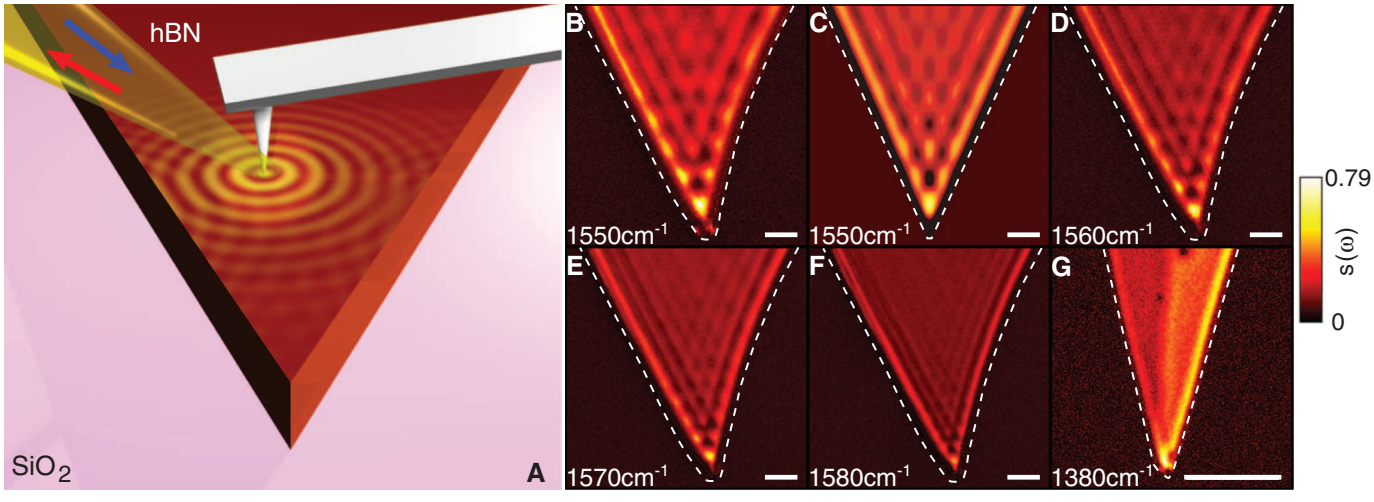

Fig. 1. Real-space imaging of surface phonon polaritons on hBN. (**A**) Schematics. Arrows denote the incident and back-scattered IR light. Concentric yellow circles illustrate the phonon polariton waves launched by the AFM tip and reflected by the two edges of a tapered hBN crystal. (**B** and **D** to **F**) IR near-field images of the normalized amplitude $s(\omega)$ defined in the text and taken at different IR frequencies [hBN thickness in (B) to (F) $d = 256$ nm]. (**C**) Simulation of the phonon polariton interference pattern (*19*). (**G**) Phonon polaritons probed in three-layer (left) and four-layer (right) hBN crystals. White dashed line tracks the hBN edges according to the AFM topography. Scale bars indicate 800 nm.

L. The nano-FTIR spectra from three representative positions are shown in Fig. 2C. Each of the frames in Fig. 2C and each pixel in Fig. 2B unveil phonon polaritons in the frequency domain. The momentum q corresponding to each ω in this map can be found from the fringe periodicity along the ω = constant cut. Therefore, a single line scan is sufficient to extract the complete dispersion profile of any surface mode.

The two approaches for mapping the surface wave dispersion produced consistent results (triangles in Fig. 2B were obtained from monochromic imaging). The broad-band line scan data (dots in Fig. 2E) allowed us to probe the dispersion in the $\omega - q$ parameter space (1430 to 1530 cm^{-1}) that cannot be investigated through the single-frequency imaging because of unavailability of proper QCLs. The experimental data for phonon polariton dispersion in Fig. 2E are in excellent agreement with the modeling results. Briefly, the surface polaritons correspond to the divergences of the reflectivity $r_p(q + i\kappa, \omega)$ of the system at complex momenta $q + i\kappa$ (*10*). For $\lambda_p \ll \lambda_{IR}$, we derived the analytical formula for polariton dispersion (*19*):

$$q(\omega) + i\kappa(\omega) = -\frac{\psi}{d}\left[\arctan\left(\frac{\varepsilon_a}{\varepsilon_\perp \psi}\right) + \arctan\left(\frac{\varepsilon_s}{\varepsilon_\perp \psi}\right) + \pi l\right], \quad \psi = \frac{\sqrt{\varepsilon_\parallel}}{i\sqrt{\varepsilon_\perp}} \qquad (1)$$

where $\varepsilon_a(\omega)$, $\varepsilon_\perp(\omega)$, $\varepsilon_\parallel(\omega)$, and $\varepsilon_s(\omega)$ are the dielectric functions of air, hBN (for directions perpendicular and parallel to the c axis), and SiO_2 substrate, respectively. The propagating modes correspond only to those integer l (if any) for which the loss factor $\gamma = \alpha\kappa/q$ is positive and less than unity. Parameter $\alpha = \pm$ is the sign of the group velocity $d\omega/dq$ (*19*). An instructive way to visualize both the dispersion and the damping is via a false-color plot of Im $r_p(q, \omega)$ (*19*, *24*) at real q and ω (Fig. 2E). Our data line up with the topmost of these curves, which corresponds to the principal $l = 0$ branch (*19*) in Eq. 1.

Additional insights into the photonic and polaritonic properties of hBN were obtained by analyzing the frequency dependence of the nano-FTIR spectra. We collected the spectrum in Fig. 2F far away from the hBN edges, where the surface waves are damped and the scattering amplitude signal is solely governed by the

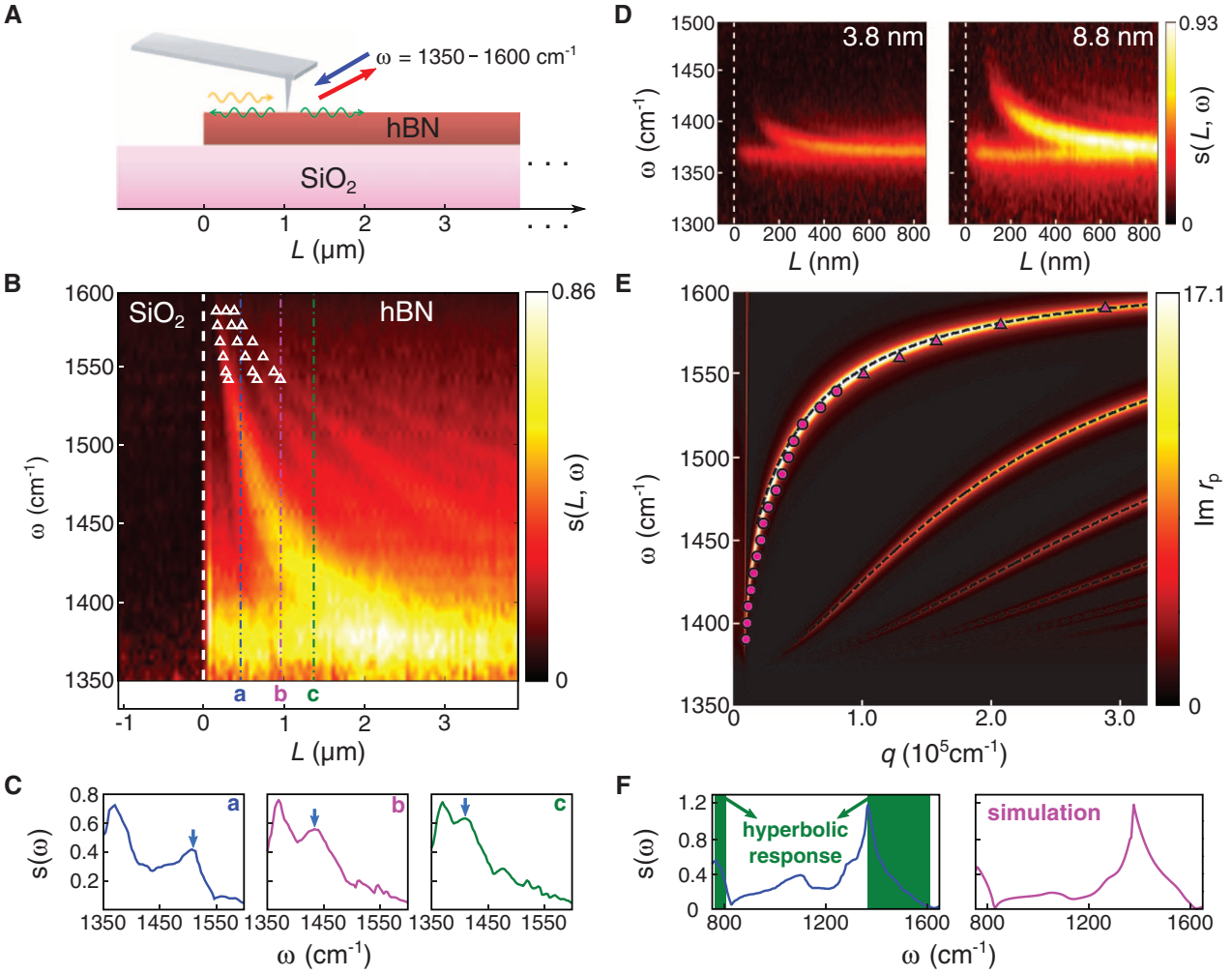

Fig. 2. The surface phonon polariton dispersion and nano-FTIR spectra. (A) Schematics of a nano-FTIR line scan across the hBN crystal. Arrows denote the incident and back-scattered IR beam spanning 1350 to 1600 cm^{-1}. Polaritonic waves are launched (green) by AFM tip and then reflected (orange) by hBN edge at $L = 0$. **(B)** Polaritonic features detected in a single line scan in (A). The normalized scattering amplitude spectra $s(\omega)$ is plotted in the false color scale. White dashed line at $L = 0$ marks the edge of the hBN crystal (thickness $d = 134$ nm). Triangles, fringe maxima extracted from monochromatic imaging similar to Fig. 1. **(C)** Nano-FTIR spectra at three representative locations along the line scan marked in (B). The peaks marked by the arrows correspond to the dominant polariton interference fringe. **(D)** Phonon polariton features as probed via line scans for ultrathin hBN crystals with $d = 3.8$ nm (left) and $d = 8.8$ nm (right). **(E)** The dispersion relation of phonon polaritons in hBN. Triangles indicate data from monochromatic imaging in Fig. 1; dots, the nano-FTIR results from (B). The data are superimposed on a false-color plot of calculated Im r_p (*19*); the black dashed lines are from Eq. 1. The straight line on the left represents the light line. **(F)** Nano-FTIR spectrum $s(\omega)$ for the hBN crystal (Fig. 1, A to F) taken away from the sample edges. The solid (green) part of the data corresponds to hBN's hyperbolic region where $\mathrm{Re}\varepsilon_\perp \cdot \mathrm{Re}\varepsilon_\parallel < 0$.

local interaction with the phonon resonances (*25*). Two of these resonances centered around 770 and 1370 cm^{-1} are due to the *c* axis and the in-plane phonon modes of hBN, respectively (*26*, *27*). The hump-dip feature around 1100 cm^{-1} originates from the SiO_2 substrate (*28*): a consequence of a partial transparency of our specimen. The quantitative relation between this spectrum, the reflectivity $r_p(q, \omega)$, and the fundamental phonon modes can be established by numerical modeling of the tip-sample interaction (*19*). The right plot of Fig. 2F indicates that our model captures the gross features of the data. Moreover, the hBN is an example of a natural hyperbolic material (*29*): a crystal possessing the in-plane and out-of-plane components of the dielectric tensor having the opposite signs so that $Re\varepsilon_{\perp} \cdot Re\varepsilon_{\parallel} < 0$. Hyperbolic regions are marked in green in Fig. 2F.

The layered nature of vdW materials, including hBN, facilitates the control of both the wavelength and the amplitude of polaritonic waves by varying the thickness *d* of the specimens. Representative line profiles (Fig. 3A) for specimens with *d* in the range of 150 to 250 nm were taken normal to the crystal edge at $L = 0$. The thickness was measured simultaneously with the scattering amplitude through the AFM topography. All fringe profiles share the same line form with a prominent peak close to the edge followed by weaker peaks that are gradually suppressed away from the edge. The oscillation period, equal to $\lambda_p/2$ (arrows in Fig. 3A), systematically decreases as the samples become thinner. This scaling extends down to a few atomic layers (Fig. 3, B and C).

The measured polariton wavelength (Fig. 3E) agrees with the theoretical predictions (Fig. 3D). For λ_p smaller than about one-half of $\lambda_{IR} = 7.1$ μm, the polariton wavelength scales linearly with the crystal thickness *d*, in agreement with Eq. 1; at larger λ_p, the linear law shows signs of saturation, also in accord with our model (Fig. 3E inset). Experimentally, the phonon polaritons display thickness-tunability persisting down to three atomic layers (Fig. 3, B and C). We detected polaritons in even thinner samples (bilayer and monolayer hBN). However, the quantitative analysis of these latter data is complicated because of the increasing role of the substrate in the polaritonic response that calls for further experiments on suspended membranes.

Similar to surface plasmons, the phonon polaritons allow one to confine and control electromagnetic energy at the nanoscale (*30*). In fact, the line form in Fig. 3A strongly resembles plasmonic standing waves in graphene (*20*, *21*). The confinement factor λ_{IR}/λ_p reaches 25 in hBN, comparable to that of plasmons in graphene (*20*, *21*). Yet these compact polaritons in hBN are able to travel at least 5 to 10 μm, compared with less than 0.5 μm for graphene plasmons. The corresponding loss factor $\gamma = \alpha\kappa/q$ is around 0.055, much smaller than a typical γ in graphene. The low damping of polaritons in our insulating samples is consistent with the absence of the electronic losses, the dominant damping channel in plasmonics. The observed losses can likely be further suppressed by improving the crystallographic order of the crystals.

Data in Figs. 1 to 3 show that phonon polaritons of the desired wavelength and confinement can be engineered by varying the number of atomic layers in hBN by, for example, exfoliation techniques. Thus, hBN and likely other polar layered materials can be integrated into vdW hetrostructures (*3*) to serve not only as electrically insulating spacers but also as waveguides for weakly damped polaritons capable of traveling over considerable distances. Additionally, the hyperbolic response of few-layer hBN is appealing in the context of unique nanophotonics characteristics of this class of solids (*29*).

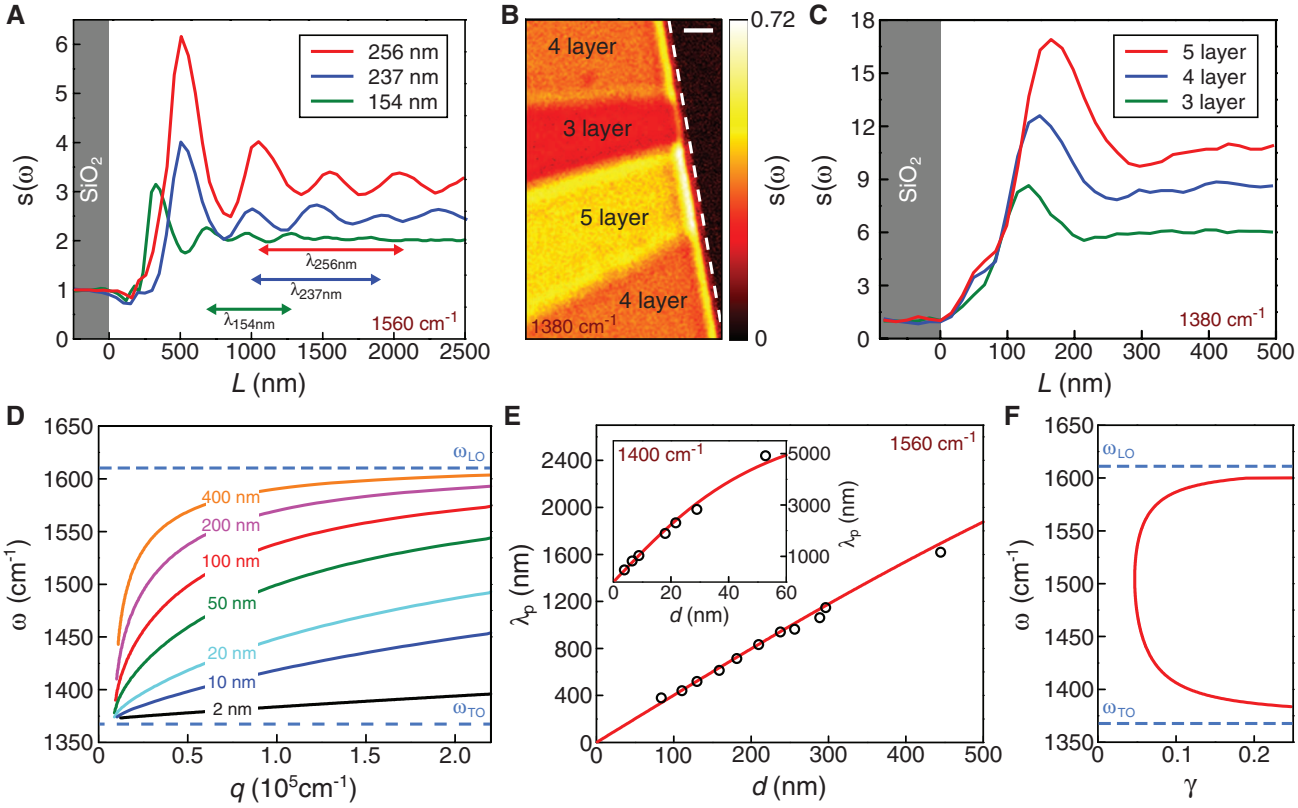

Fig. 3. The evolution of the phonon polariton wavelength and amplitude with the thickness of hBN crystals. (**A**) Line profiles of the scattering amplitude $s(\omega)$ at 1560 cm^{-1} for hBN crystals with $d = 154$, 237, and 256 nm. Arrows indicate the polariton wavelength. (**B**) Near-field image and (**C**) phonon polariton line profiles for few-layer hBN crystals. White dashed line in (B) tracks the sample boundary; scale bar in (B), 400 nm. (**D**) Calculated dispersion relation of the $l = 0$ branch of the phonon polaritons in hBN for various crystal thicknesses (*d*). TO and LO frequencies are marked with blue dashed lines. (**E**) Dots, wavelengths of phonon polaritons probed at 1560 cm^{-1} for crystals with different thicknesses (*d*); red line, calculated thickness-dependence relation. (Inset) Thickness-dependence relation probed at 1400 cm^{-1} for ultrathin hBN crystals. See (*19*) for details. (**F**) Calculated loss factor for phonon polaritons.

References and Notes

1. C. R. Dean *et al.*, *Nat. Nanotechnol.* **5**, 722–726 (2010).
2. K. S. Novoselov *et al.*, *Proc. Natl. Acad. Sci. U.S.A.* **102**, 10451–10453 (2005).
3. A. K. Geim, I. V. Grigorieva, *Nature* **499**, 419–425 (2013).
4. T. Kimura, Y. Tokura, *Annu. Rev. Mater. Sci.* **30**, 451–474 (2000).
5. K. F. Mak, C. Lee, J. Hone, J. Shan, T. F. Heinz, *Phys. Rev. Lett.* **105**, 136805 (2010).
6. A. Splendiani *et al.*, *Nano Lett.* **10**, 1271–1275 (2010).
7. X. Qi, S. Zhang, *Rev. Mod. Phys.* **83**, 1057–1110 (2011).
8. L. Britnell *et al.*, *Science* **340**, 1311–1314 (2013).
9. S. Z. Butler *et al.*, *ACS Nano* **7**, 2898–2926 (2013).
10. L. Novotny, B. Hecht, *Principles of Nano-Optics* (Cambridge Univ. Press, Cambridge, 2006).
11. J. Renger, S. Grafström, L. M. Eng, R. Hillenbrand, *Phys. Rev. B* **71**, 075410 (2005).
12. S. Shen, A. Narayanaswamy, G. Chen, *Nano Lett.* **9**, 2909–2913 (2009).
13. T. Feurer, J. C. Vaughan, K. A. Nelson, *Science* **299**, 374–377 (2003).
14. Y. De Wilde *et al.*, *Nature* **444**, 740–743 (2006).
15. A. Huber, N. Ocelic, D. Kazantsev, R. Hillenbrand, *Appl. Phys. Lett.* **87**, 081103 (2005).
16. T. Taubner, D. Korobkin, Y. Urzhumov, G. Shvets, R. Hillenbrand, *Science* **313**, 1595 (2006).
17. G. Shvets, *Phys. Rev. B* **67**, 035109 (2003).
18. J. A. Schuller, R. Zia, T. Taubner, M. L. Brongersma, *Phys. Rev. Lett.* **99**, 107401 (2007).
19. Materials and methods are available as supplementary materials on *Science* Online.
20. J. Chen *et al.*, *Nature* **487**, 77–81 (2012).
21. Z. Fei *et al.*, *Nature* **487**, 82–85 (2012).
22. F. Keilmann, S. Amarie, *J. Infrared Millimeter Terahertz Waves* **33**, 479–484 (2012).
23. J. M. Atkin, S. Berweger, A. C. Jones, M. B. Raschke, *Adv. Phys.* **61**, 745–842 (2012).
24. Z. Fei *et al.*, *Nano Lett.* **11**, 4701–4705 (2011).
25. R. Hillenbrand, T. Taubner, F. Keilmann, *Nature* **418**, 159–162 (2002).
26. R. Geick, C. H. Perry, G. Rupprecht, *Phys. Rev.* **146**, 543–547 (1966).
27. X. G. Xu, A. E. Tanur, G. C. Walker, *J. Phys. Chem. A* **117**, 3348–3354 (2013).
28. L. M. Zhang *et al.*, *Phys. Rev. B* **85**, 075419 (2012).
29. A. Poddubny, I. Iorsh, P. Belov, Y. Kivshar, *Nat. Photonics* **7**, 948–957 (2013).
30. R. Stanley, *Nat. Photonics* **6**, 409–411 (2012).

Acknowledgments: Work at UCSD was supported by U.S. Department of Energy–Office of Basic Energy Sciences (DOE-BES). The development of nano-FTIR at UCSD is supported by Office of Naval Research (ONR), DOE, Air Force Office of Scientific Research (AFOSR), and NSF. M.M.F. is supported by ONR. P.J.-H. acknowledges support from AFOSR grant number FA9550-11-1-0225. A.S.R. acknowledges DOE grant DE-FG02-08ER46512 and ONR grant MURI N00014-09-1-1063. M.T. and G.D. are supported by NASA. A.H.C.N. acknowledges a National Research Foundation–Competitive Research Programme award (R-144-000-295-281). A.Z., W.G., and W.R. acknowledge support from the Director, Office of Energy Research, BES, Materials Sciences and Engineering Division, of the U.S. DOE under contract no. DE-AC02- 05CH11231, which provided for preparation and characterization of the BN, and from the ONR, which provided for substrate transfer technique. F.K. is a cofounder of Neaspec, producer of the s-SNOM apparatus used in this study.

Supplementary Materials

www.sciencemag.org/content/343/6175/1125/suppl/DC1
Materials and Methods
Supplementary Text
Figs. S1 to S5
References (*31*–*42*)

4 October 2013; accepted 6 February 2014
10.1126/science.1246833

Rapid Reductions in North Atlantic Deep Water During the Peak of the Last Interglacial Period

Eirik Vinje Galaasen,[1]* Ulysses S. Ninnemann,[1,2] Nil Irvalı,[2] Helga (Kikki) F. Kleiven,[1,2] Yair Rosenthal,[3] Catherine Kissel,[4] David A. Hodell[5]

Deep ocean circulation has been considered relatively stable during interglacial periods, yet little is known about its behavior on submillennial time scales. Using a subcentennially resolved epibenthic foraminiferal $\delta^{13}C$ record, we show that the influence of North Atlantic Deep Water (NADW) was strong at the onset of the last interglacial period and was then interrupted by several prominent centennial-scale reductions. These NADW transients occurred during periods of increased ice rafting and southward expansions of polar water influence, suggesting that a buoyancy threshold for convective instability was triggered by freshwater and circum-Arctic cryosphere changes. The deep Atlantic chemical changes were similar in magnitude to those associated with glaciations, implying that the canonical view of a relatively stable interglacial circulation may not hold for conditions warmer and fresher than at present.

Future climate could be affected on a global scale if the circulation of North Atlantic Deep Water (NADW), the main water mass ventilating the deep Atlantic (Fig. 1) (*1*), is altered. Such changes could have widespread and long-lasting impacts—including, for example, on regional sea level (*2*), the intensity and pacing of Sahel droughts (*3*), and the pattern and rate of ocean acidification and CO_2 sequestration (*4*). However, the response of NADW to high-latitude warming and ocean freshening, both of which would decrease source region density and potentially inhibit NADW formation, remains a key uncertainty in future climate projections. Model estimates range from nearly no change to ~50% reduction in Atlantic Meridional Overturning Circulation by 2100 CE (*5*). Compounding the uncertainty, models may inherently underestimate the possibility for abrupt and large changes (*6*), and there may even be critical stability thresholds in surface ocean buoyancy that, if crossed, could switch circulation into an equilibrium state without strong NADW formation (*7*, *8*). The current consensus is that we are far from any such stability thresholds and that the modern style of vigorous NADW ventilation is a robust feature of warm interglacial climates. Only modest millennial-scale NADW variability has been found to occur during interglacials (*9*, *10*) relative to that seen during colder glacial periods (*11*). However, large but shorter-lived transient anomalies might be possible even in the midst of a generally vigorous interglacial circulation (*7*, *12*, *13*). Hence, reconstructions with appropriate resolution to characterize the short-term instability of NADW during warmer climates are needed to assess model fidelity and constrain possible tipping points for ocean circulation. We used deep sea sediment proxy records from key locations (Fig. 1) to assess the occurrence and magnitude of centennial-scale variability in NADW over the warm interval of the last interglacial period (LIG) [marine isotope stage (MIS) 5e]. The LIG is a useful period for evaluating the sensitivity of NADW to key features that we may face in the future, including a warmer and fresher North Atlantic than at present (*14*, *15*) and the retreat of the circum–North Atlantic cryosphere (*15*, *16*).

We characterized the short-term variability of NADW over the LIG using sediment core MD03-2664 (57°26.34′N, 48°36.35′W; 3442 m water depth) from the Eirik Drift site used to identify the centennial-scale NADW reduction associated with the climate anomaly 8.2 thousand years before the present (ky B.P.) (*12*). This site monitors the newly formed, integrated Nordic Seas overflows (*12*) that are the primary constituents of lower NADW (*1*). The high sedimentation rate (~35 cm ky^{-1}) at this location allows a multidecadal depiction of lower NADW properties and ventilation across the LIG (~30 years per 1-cm sample), which is approximately an order of magnitude greater than the previous reconstructions used to infer millennial-scale NADW stability during the LIG (*10*, *17*).

On our age model (*18*), the MIS 5e "plateau" [the interval of relatively constant minimum ice volume (benthic $\delta^{18}O$)] corresponds to 116.1 to 128.0 ky. We focused our study on this interval, referring to it as the LIG. We documented NADW variability using the carbon isotopic composition

[1]Department of Earth Science, University of Bergen and Bjerknes Centre for Climate Research, Allégaten 41, 5007 Bergen, Norway. [2]Uni Climate, Uni Research and Bjerknes Centre for Climate Research, Bergen, Norway. [3]Institute of Marine and Coastal Sciences and Department of Earth and Planetary Sciences, Rutgers University, New Brunswick, NJ, USA. [4]Laboratorie des Sciences du Climat et de l'Environnement/Institut Pierre Simon Laplace, CEA/CNRS/UVSQ, Gif-sur-Yvette, France. [5]Godwin Laboratory for Paleoclimate Research, Department of Earth Sciences, University of Cambridge, Cambridge, UK.

*Corresponding author. E-mail: eirik.galaasen@geo.uib.no